Methods and Applications in Fluorescence

PAPER

Influence of polyvinylpyrrolidone (PVP) in the synthesis of luminescent $NaYF_4$:Yb,Er upconversion nanoparticles

Ross Birch[1,5], **Jochen Bruckbauer**[2,5], **Marta Gajewska**[3], **Grzegorz Cios**[3], **Robert Pal**[4] and **Lewis E MacKenzie**[1,*]

[1] Department of Pure and Applied Chemistry, University of Strathclyde, Glasgow, G1 1RD, United Kingdom
[2] Department of Physics, SUPA, University of Strathclyde, Glasgow, G4 0NG, United Kingdom
[3] Academic Centre of Materials and Nanotechnology, AGH University of Science and Technology, Kraków, 30-059, Poland
[4] Department of Chemistry, Durham University, Durham, DH1 3LE, United Kingdom
[5] These authors are credited with joint first-authorship due to equivalent contributions.
[*] Author to whom any correspondence should be addressed.

E-mail: l.mackenzie@strath.ac.uk

Keywords: upconversion nanoparticles, synthesis, polyvinylpyrrolidone (PVP), luminescence, $NaYF_4$:Yb, Er $NaYF_4$:Yb, Tm

OPEN ACCESS

RECEIVED
22 December 2022

REVISED
11 May 2023

ACCEPTED FOR PUBLICATION
23 May 2023

PUBLISHED
30 May 2023

Abstract

Polyvinylpyrrolidone (PVP) can be used to produce upconversion nanoparticles (UCNPs) in an advantageous manner, i.e. at modest temperatures in open-to-air conditions with simple hotplate and flask apparatus. However, the influence of PVP parameters on the formation of UCNPs has not been previously investigated. In this exploratory study, we establish that PVP molecular weight and relative amount of PVP can greatly influence the morphology and diameter of $NaYF_4$:Yb,Er UCNPs produced via the PVP-assisted route. At nominal amounts of PVP, varying the molecular weight of PVP in synthesis between 10,000 g mol^{-1} (PVP10), 40,000 g mol^{-1} (PVP40), and 55,000 g mol^{-1} (PVP55), had minimal effect on UCNP morphology, whereas reducing the quantity of PVP10 and PVP40 in the reaction to 10% of the nominal amount resulted in two notable effects: (1) the generation of a greater range of UCNP diameters and (2) the production of an unexpected sub-population of rhombus-shaped UCNPs. Bulk and individual nanoparticle analysis indicates that all UCNP morphologies were cubic (α-phase) crystal structure and consisted of $NaYF_4$:Yb,Er. Optical emission properties exhibited only modest green and red luminescence emission ratio when PVP parameters were varied. However, separately produced PVP40 $NaYF_4$:Yb,Tm UCNPs exhibited a much more intense and dual-band blue/red emission. This exploratory work demonstrates that tailoring PVP content in synthesis of UCNPs can greatly alter morphology of UCNPs produced and should be carefully considered in experimental design. However, the underlying mechanisms of action of the role PVP plays in this synthesis remain unclear. Ultimately, significant further work is still required to fully elucidate the relevant chemistry to achieve full control of PVP-UCNP synthesis.

1. Introduction

Polyvinylpyrrolidone (PVP) (see figure 1(a)) is a versatile polymer which fulfils a variety of purposes in colloidal nanoparticle synthesis: it is a reducing agent, it can control nanoparticle growth, and it can stabilize nanoparticle surfaces. The PVP monomer contains both a hydrophobic alkyl group and a hydrophilic pyrrolidone moiety, enabling PVP-capped nanoparticles to be dispersed in a wide range of organic solvents and water [1]. PVP has been utilized in the synthesis of a wide range of nanoparticles and nanostructures, e.g. Koczkur *et al* (2015) note the use of PVP in the synthesis of Au, Ag, Pd, Pt, bimetallic, metal oxide, and metal chalcogenide nanostructures [1]. Varying PVP molecular weight and relative amount in synthesis has been demonstrated to alter the morphology of nanoparticles produced, e.g. by encouraging growth along specific crystal facets [1, 2]. Koczkur *et al* (2015) also noted that manipulation of PVP in synthesis can give rise to a wide variety of nano-morphologies, including nano-wires, cubes, plates, arrow-headed tripods, nano-flowers, nano-cages, tetrahedra, hexagon, polyhedral, and triangular morphologies [1].

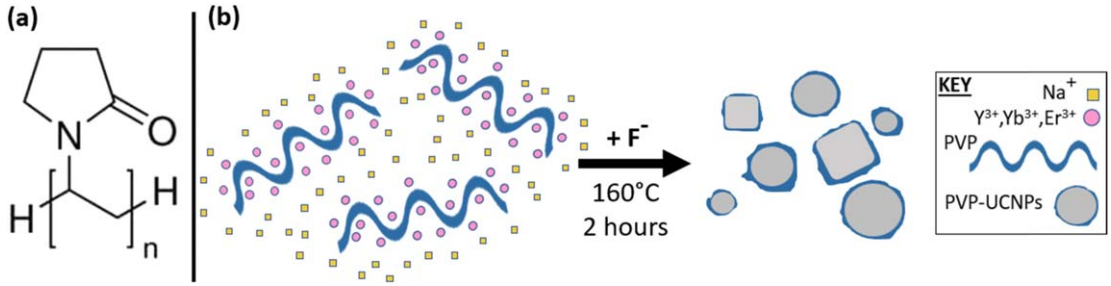

Figure 1. Polyvinylpyrrolidone (PVP) in UCNP synthesis. (a) Structure of PVP. (b) The reaction model proposed by Li and Zhang (2006) [3], where Ln^{3+} ions (Y^{3+},Yb^{3+},Er^{3+}) associate the PVP prior to the addition of F^- ions, which leads to formation of PVP-UCNPs.

Xia *et al* (2011) [2], provide an excellent example, where reducing PVP quantity in synthesis enabled control of the morphology of Ag nanoparticles grown via seeds, with cubic, intermediate, and octahedral morphologies accessible by varying PVP concentration [2]. Since the mid-2000s, PVP has sporadically been used in the synthesis of upconversion nanoparticles (UCNPs) [3–6], offering a simple, low-cost and robust synthesis route that can be advantageous in comparison to alternative high-pressure and oxygen-free techniques, especially for larger-scale UCNP production. However, the potential influence of PVP molecular weight and PVP amount in synthesis on the morphology and optical properties of PVP-UCNPs has not yet been investigated.

UCNPs are crystalline nanoparticles, typically consisting of a low-phonon energy crystalline host lattice (e.g. $NaYF_4$, $NaLuF_4$, KYb_2F_7, $BaYF_5$, $LiYF_4$, SrF_2, ZrO_2, YVO_4, $Ca_3(PO_4)_2$, etc) with photonically-active rare Earth dopants [7–16]. The crystal structure and optical properties of that rare Earth dopants enables UCNPs to convert multiple low-energy near-infrared photons into higher-energy visible photons. UCNP emission is tuneable, and is primarily dependent on the core UCNP structure and choice of photonically active rare-Earth (*f*-block) (e.g. Yb^{3+}, Gd^{3+}, Er^{3+}, Tm^{3+}, Nd^{3+}) and transition metal (*d*-block) elements (e.g. Mn^{2+}, Fe^{3+}) incorporated within the UCNPs [17–20]. Unlike conventional organic fluorophores, UCNPs are resilient again photo bleaching, and the near-infrared excitation has very low phototoxicity and does not induce visible autofluorescence in biological samples. Additionally, the surface of UCNPs can be altered with various coatings to enhance biocompatibility and enable biological targeting [21]. As such, UCNPs are uniquely suited for biomedical applications, such as cellular labelling, biosensing, and deep-tissue photodynamic therapy [21–24]. Additionally, UCNPs also find utility in display screen technologies, extreme-temperature thermometry, light-harvesting for solar cells, and as components of advanced security inks [25–33].

Synthesis of UCNPs has been historically challenging, presenting a considerable barrier to entry for researchers new to the field. For example, solvothermal and hydrothermal reactions require a high-pressure sealed autoclave capable of withstanding elevated pressures at temperatures typically up to 200 °C, whereas 'hot injection' methods require oxygen-free reactions at ∼300 °C for extended reaction times. These reaction conditions are hazardous and warrant skilled operation and careful risk mitigation. Furthermore, these techniques are very sensitive to variables such as reaction time, pH, and the ratio of solvents/coordinating ligands used [12]. Therefore, reproducibility between different research groups can be challenging [34]. Ultimately, despite their near ubiquity in the field, these solvothermal/hydrothermal synthesis and hot injection synthesis are specialist synthesis methods, which are resource, expertise, and energy intensive, which are a barrier to entry for researchers, and which are ultimately challenging to scale-up [35]. Microwave-assisted synthesis provides an attractive route for straight-forward UCNP synthesis, with excellent prospects for *in situ* monitoring and batch reactions, but this requires specialist microwave reactor equipment [36–38]. Notably, some methods for producing UCNP materials at low temperatures (<50 °C) with simple equipment have been reported, but these studies only report upconversion properties in dry solid or dry powdered states [39, 40]. Therefore there is a need for a more straight-forward and cost-effective method to synthesise water and solvent-dispersible UCNPs, especially for large-scale applications such as security inks, solar cells, and display technologies [17]. The PVP-assisted UCNP synthesis route provides a solution to these issues.

The PVP-assisted route has sporadically attracted attention since its innovation by Li and Zhang in 2006 (see figure 1(b)) [3]. It requires only modest-temperatures (160 °C), a single solvent, can be conducted open-to-air, and requires only simple hotplate and beaker apparatus. As such the PVP-assisted method can be deployed easily, and is a promising candidate for directly scaled-up or batch-parallelised UCNP production, which would be particularly advantageous for applications requiring bulk quantities of

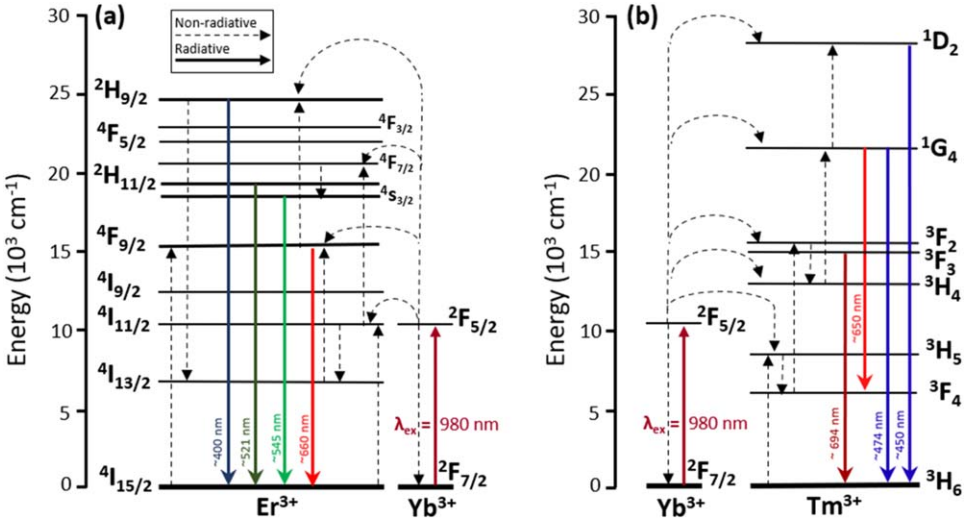

Figure 2. Energy level for the upconversion processes relevant to this study. (a) Upconversion in $NaYF_4$:Yb,Er UCNPs. (b) Upconversion in $NaYF_4$:Yb,Tm UCNPs [17, 45].

UCNPs, such as display screens and for advanced security inks [26, 27, 30–33, 41, 42].

In the PVP-assisted method, it is speculated that the various trivalent lanthanide ions nucleate to the pyrrolidone moieties of PVP (see figure 1(b)) [1, 43], with the subsequent addition of F^- ions causing the formation of the $NaYF_4$:Yb,Er crystalline lattice. PVP then acts to constrain the size of the resultant UCNPs, and to aid dispersal in solvents. Typical UCNP reaction time is 2 h and produces ~130 mg of PVP-UCNPs. To date, red/green (Yb^{3+},Er^{3+}), strong red (Yb^{3+},Er^{3+},Mn^{2+}), and blue emitting (Yb^{3+},Tm^{3+}) UCNPs have been produced with the PVP-assisted route [3, 17], but other emission wavebands may be accessible by incorporating different dopant combinations [18].

The PVP-assisted UCNP production method has been utilized to produce cubic (α-phase) $NaYF_4$:Yb,Er UCNPs for various purposes, including sub-cellular microscopy, drug delivery, MRI imaging, and light harvesting in solar cells [5, 6, 29, 44]. Typically the $NaYF_4$:Yb,Er UCNPs which are produced using a nominal quantity of PVP40 in the synthesis (i.e. 574 mg) are approximately 40 to 50 nm in diameter (depending on diameter quantification method), exhibit a ~1:1 emission ratio for red/green Er^{3+} emission wavebands (see figure 2 for a corresponding energy level diagram), and a crystal lattice parameter, *a*, of 5.52 Å which has been reproducible between studies [6, 17]. Furthermore, PVP-UCNPs can be functionalised with silica shells to mitigate solvent quenching or mesoporous silica shells for functional molecular loading [3, 5, 45].

Recently, our group has established that the PVP-assisted method can produce cubic (α-phase) $NaYF_4$:Yb,Er,Mn UCNPs with remarkably enhanced red emission [17]. The sixfold increase in red emission was attributed to incorporation of Mn^{2+} co-doping resulting in (1) a reduced crystal lattice parameter (i.e. from 5.52 Å to 5.45 Å); (2) three-photon sensitized upconversion; and (3) reduced nanoparticle diameter (i.e. 36 ± 15 nm maximum Feret diameter), potentially attributable to recently discovered crystal lattice strain effects recently reported by Quintanilla *et al* (2022) [46], but this is not verified. Overall, the PVP-assisted route is an attractive method for synthesis of UCNPs with various luminescence emission properties, albeit a method which has not been well utilized by the wider research community.

To-date, the influence of key variables in the PVP-assisted route of UCNP synthesis have not been established. The majority of studies have used a single PVP molecular weight (i.e. PVP40, with a molecular weight of 40,000 g mol^{-1}) and (a seemingly arbitrary) fixed quantity of PVP (~574 mg/14 μmols). The singular exception known to us is the study by Meng *et al* (2012), who report using 500 mg of PVP K-30 (molecular weight of 58,000 g mol^{-1}), i.e. 8.6 μmols of PVP K-30,to produce $NaYF_4$ nanoparticles with unspecified diameter distributions [29]. We hypothesised that altering the amount and molecular weight of PVP in UCNP synthesis would influence UCNP morphology [45]. As such, the aim of this initial exploratory study was to establish what influence of PVP molecular weight and PVP quantity may have on UCNPs produced via this PVP-assisted low-temperature open-air synthesis method. For this initial exploratory study, we reduced the amount of PVP in the synthesis to an arbitrary value of 10%, i.e. an order of magnitude less than the nominal amount. As a point of comparison, Xia *et al* (2011) [2] found that a similar reduction of PVP amount to 10% nominal values was a critical threshold for producing Ag nanoparticles with different morphologies [2]. We selected $NaYF_4$:Yb,Er UCNPs as our model nanoparticle system because it is a commonly used and well-studied UCNP

Table 1. Variables changed in synthesis of each UCNP sample.

UCNP sample	Dopant composition	PVP molecular weight ($g\,mol^{-1}$)	Total mass of PVP used in synthesis (mg)	Total dry weight of UCNPs produced (mg)
	(mol %) of 1 mmol			
PVP40 Tm^{3+}	$Y^{3+} = 78$	40,000	574.0	134 ± 5
	$Yb^{3+} = 20$			
	$Tm^{3+} = 2$			
10% PVP10 Er^{3+}	$Y^{3+} = 78$	10,000	57.4	65 ± 4
	$Yb^{3+} = 20$			
	$Er^{3+} = 2$			
PVP10 Er^{3+}	$Y^{3+} = 78$	10,000	574.0	89 ± 5
	$Yb^{3+} = 20$			
	$Er^{3+} = 2$			
10% PVP40 Er^{3+}	$Y^{3+} = 78$	40,000	57.4	113 ± 5
	$Yb^{3+} = 20$			
	$Er^{3+} = 2$			
PVP40 Er^{3+}	$Y^{3+} = 78$	40,000	574.0	117 ± 5
	$Yb^{3+} = 20$			
	$Er^{3+} = 2$			
10% PVP55 Er^{3+}	$Y^{3+} = 78$	55,000	57.4	88 ± 5
	$Yb^{3+} = 20$			
	$Er^{3+} = 2$			
PVP55 Er^{3+}	$Y^{3+} = 78$	55,000	574.0	125 ± 6
	$Yb^{3+} = 20$			
	$Er^{3+} = 2$			

composition, which minimises the variables involved and assists in inter-study comparisons.

2. Methods

2.1. Synthesis of UCNPs

PVP-UCNPs were produced as per a recent study by our group [17], which in-turn was adapted from prior studies [3, 5, 6]. In brief, yttrium (III) oxide [Y_2O_3] (99.99%), ytterbium (III) oxide [Yb_2O_3] (99.9%), erbium (III) oxide [Er_2O_3] (99.9%), thulium (III) oxide [Tm_2O_3] (99.9%), PVP10 (10,000 $g\,mol^{-1}$), PVP40 (40,000 $g\,mol^{-1}$), PVP55 (55,000 $g\,mol^{-1}$), sodium chloride (>99.5%, BioXtra), and ammonium fluoride [>99.99%] (NH_4F) were purchased from Merck Life Science Ltd 70% nitric acid (HNO_3), ethylene glycol [$(CH_2OH)_2$] (>99% extra pure ACROS Organics), absolute ethanol [EtOH] (>99.8%) were purchased from Fisher Scientific UK Ltd All materials were subsequently used without further purification.

5X stock solutions of Y_2O_3 [44.0 $mg\,ml^{-1}$], Yb_2O_3 [19.7 $mg\,ml^{-1}$], Er_2O_3 [1.92 $mg\,ml^{-1}$], and Tm_2O_3 [1.93 $mg\,ml^{-1}$], were prepared in 10 ml of 10% HNO_3 and allowed to dissolve completely (N.B. this take several days for Y_2O_3, Yb_2O_3 stocks due to the relatively higher concentration required and poor solubility of these oxides in 10% HNO_3). Stock solutions of NH_4F (74.1 $mg\,ml^{-1}$) and the various PVP molecular weights and amounts (287 $mg\,ml^{-1}$ PVP for preparation of nominal PVP samples, and 28.7 $mg\,ml^{-1}$ for 10% PVP samples) were prepared in ethylene glycol at least 24 h in advance at room temperature, with PVP stocks being vigorously stirred by hand using a glass rod for 5 min to aid dissolution in the viscous solution.

Synthesis required the preparation of two mixtures. For mixture A, appropriate amounts of each Ln^{3+} stock solution (typically ~2 ml each) were then combined in a 50 ml beaker to create a solution containing a total of 1 mmol of Ln^{3+} ions of various ratios (see table 1). This solution was stirred vigorously for one minute and then heated to 120 °C using a hotplate/stirrer to evaporate the aqueous content. This was deemed complete when the transparent residue (consisting of lanthanide nitrates[3, 17]) at the bottom of the beaker stopped bubbling. 8 ml of ethylene glycol was then added, and the solution heated to 80 °C whilst being stirred for 30 min Whilst maintaining temperature at 80 °C, 58.5 mg (1 mmol) of NaCl was then added directly to the solution and stirred for a further 5 min 2 ml of the appropriate PVP stock (see table 1) was then added, and the solution stirred for a further 10 min, after which the solution was transferred to an open-necked round bottom flask and maintained at 80 °C via a silicone oil bath heated by a hotplate/stirrer with thermocouple (Fisherbrand™ AREX with VTF, 630 W, maximum temperature 370 °C, aluminium alloy heating plate 15.5 cm diameter). For mixture B, 8 ml of ethylene glycol was added to a 50 ml conical flask and heated to 80 °C. 2 ml of 74.1 $mg\,ml^{-1}$ NH_4F stock (i.e. 4 mmol) was then added and stirred for 10 min. Mixture B was then added to mixture A dropwise and stirred at 80 °C for 10 min. The resultant solution was then heated to 160 °C using the silicon oil bath and the hotplate stirrer at

full power. In all instances the temperature of the solutions was measured directly by placing the hotplate/stirrer thermocouple directly in the reaction mixture. The solution was maintained at 160 °C for 2 h, during which UCNPs formed, with the reaction progressing from opaque white to an opaque yellow/orange colouration, likely due to formation of NO_2 from decomposition of nitrates. The UCNPs were then pelleted by centrifugation at 10,000 relative centrifugal force (RCF) for 30 min; the supernatant was removed and replaced with 10 ml of fresh EtOH; the UCNPs were then resuspended by sonication for 15 min. Subsequently two more wash steps were conducted as per the first wash step; UCNPs were then suspended in a final volume of 5 ml EtOH and stored at room temperature in sealed 50 ml falcon tubes.

2.2. UCNP characterisation

2.2.1. Quantifying sample weight

The dry weight of UCNPs produced in each sample was estimated by first pre-weighing empty open glass vials with a high precision (0.1 mg) balance five times (to quantify random error), then sonicating the UCNP samples for 10 min prior to transferring 500 μl of each UCNP sample into the vials within a ventilated fumehood, and subsequently allowing the EtOH to evaporate naturally. The vials were then weighed five times. Uncertainties were extrapolated from the standard deviation of five measurements combined with manufacturer's quoted random error of the pipette used (Gilson Pipeteman® Classic P1000), i.e. ± 1 μl.

2.2.2. Electron microscopy and UCNP diameter analysis

For scanning transmission electron microscopy (STEM), the as-prepared samples were sonicated for 10 min, then 20 μl of each UCNP sample was added to 1.98 ml of isopropyl alcohol and sonicated for 1 min. For each sample, a fresh grid (holey carbon film on 200 mesh, Agar Scientific Ltd) was gripped using tweezers and then dipped into the UCNP solution and the grid was allowed to dry via evaporation at room temperature. Samples were stored in a grid box. Each individual sample was then placed onto a single sample stage and affixed using conductive silver paint. Each sample was imaged in STEM mode using a variable pressure field emission gun scanning electron microscope (FEI Quanta 250) operating in high vacuum mode with an accelerating voltage of 30 kV at a working distance of ~6 mm, at 100,000X magnification, and using a two-segment solid-state detector holder operating in bright-field mode, mounted under the sample. The diameter of UCNPs was estimated by importing STEM images acquired at 100,000X magnification into ImageJ [47, 48] and manually measuring the maximum and minimum Feret diameters of ~80–120 randomly selected UCNPs in each sample.

For scanning electron microscopy (SEM), the as-prepared samples were sonicated for 10 min then 20 μl of the as-prepared UCNP samples was added to 1.98 ml of isopropyl alcohol and sonicated for 1 min. Silicon wafer fragments were placed on a 50 °C hotplate and washed with 20 μl of isopropyl alcohol which was allowed to evaporate. Once dry, a single drop (~10 μl) of the diluted UCNP sample was placed on the silicon wafer fragment and allowed to evaporate. Once dry, the silicon wafers were mounted to aluminium specimen stubs using adhesive carbon tabs and stored in a stub box. The stubs were then mounted on a multi-stub sample holder and imagined using the aforementioned SEM operating in high vacuum mode with an accelerating voltage of 10 kV, at a working distance of ~6 mm, at 100,000X magnification, and using the standard secondary electron (SE) detector. For both STEM and SEM, images were saved in uncompressed .TIF format at a resolution of 1024 × 943 pixels.

Further high-resolution transmission electron microscopy (HR-TEM) of selected samples was performed using a Tecnai TF 20 X-TWIN microscope (FEI). Elemental mapping analysis was performed using an energy dispersive spectrometer (EDS r-TEM, EDAX) under an accelerating voltage of 200 kV. Samples were prepared as per STEM imaging.

2.2.3. Structure analysis via transmission Kikuchi diffraction (TKD)

Transmission Kikuchi diffraction (TKD), also referred to transmission electron backscatter diffraction (t-EBSD) [49, 50] was performed in a field emission gun SEM (FEI Versa 3D) equipped with an Oxford Instruments Symmetry S2 EBSD detector. For TKD, the samples were prepared on a carbon mesh grid using the same steps as described above for the STEM measurements. The mesh grid was mounted at −60° on custom-built TKD holder, as described in Tokarski *et al* (2021) [51]. The stage was tilted by 40° to result in sample tilt of −20° which is typical for off-axis TKD measurements. TKD measurements were carried out at an acceleration voltage of 30 kV using EBSD camera settings of 'Speed 1' (622 × 512 pixels) or 'Speed 2' (156 × 128 pixels) and a gain setting of 2. TKD maps were acquired with a step size of 10 nm. Oxford Instrument's Refined Accuracy method was used for indexing the TKD patterns with increased angular resolution. Subsequent, TKD analysis was carried out using the Matlab-based toolbox MTEX [52], which was also used to produce TKD maps. Dark field STEM images were recorded in forescatter electron detector (FSD) geometry using solid state diodes placed around the EBSD detector screen.

2.2.4. Structure analysis via powder x-ray diffraction (PXRD)

Dry powder samples were prepared by decanting ~10 mg of UCNPs in EtOH into an open clean glass vial inside a ventilated fume hood and allowing the EtOH to evaporate naturally at room temperature.

Afterwards, the dry residue was scraped with a clean spatula within the vial to form a white powder. The samples were then placed into a Kapton-backed multi-well sample holder. PXRD measurements were obtained using a D8 Discover (Bruker Corporation) x-ray diffractometer using a Cu Kα x-ray source ($\lambda = 1.5406$ Å) and scanning 2Θ angles between 10° and 90° in 0.017° increments at a rate of 0.5 s per increment. After acquisition, the background of each PXRD pattern was removed using the background subtraction function of *Diffrac.eva* software (Bruker Corporation). PXRD peaks were indexed by comparison to reference pattern data. The position of each peak was calculated using custom-written Matlab script (Matlab 2021b, Mathworks). The cubic (α-phase) crystal lattice parameter, a, was calculated from each peak by:

$$d_{hkl} = \frac{\lambda}{2\sin(2\theta/2)} \quad (1)$$

$$a_{hkl} = d_{hkl}\sqrt[2]{h^2 + k^2 + l^2} \quad (2)$$

where λ is the wavelength of the x-ray source, d_{hkl} is the interplanar spacing associate with a given PXRD peak, hkl are the Miller indices corresponding to each peak, and 2Θ is the two-theta angle of each peak. Uncertainties in a were quantified by the standard deviation of eight estimates of a from eight PXRD peaks.

2.2.5. Elemental composition analysis via inductively coupled plasma mass spectroscopy (ICP-MS)

Dry powder UCNP samples as per 2.2.4. were prepared in 2 ml Eppendorf tubes. One ml of ultra-pure water (resistivity of 18.2 MΩ) was added to each sample, then the sample was transferred into a perfluoroalkoxy alkane (PFA) microwave digestion tube (MARS Xpress 75 ml) via a pipette. To remove any possible remains of the sample from the sample tube, the procedure was repeated with 1 ml concentrated hydrochloric acid (HCl, 37%, Trace Metal Grade, Fisher Chemical); then with 1 ml concentrated nitric acid (HNO_3, 67%, Trace Metal Grade, Fisher Chemical). An additional 1 ml of HCL and 3 ml of HNO_3, was then directly added into microwave digestion tube. Samples were acid digested using a Microwave Assisted Reaction System (MAE, MARS-5, CEM Corporation), following the microwave operating parameters: operating power 800 W; ramp for 20 min up to 200 °C; hold time 20 min at 200 °C. Samples digests were brought up to 50 ml in volumetric flasks using ultra-pure water (18.2 MΩ resistivity) and then filtered through 0.45 μm cellulose acetate syringe filter (Millex). Samples were then diluted by 100X prior to inductively coupled plasma mass spectrometry (ICP-MS) analysis using an Agilent 7700X system running MasSunter B.01.01 software. For calibration, a custom standard solution from QMX laboratories was used. The standard solution (Lot No 815774, Ref No Q167638) consisted of Na^+, Y^{3+}, Yb^{3+}, Er^{3+}, and Tm^{3+} at a concentration of 100 mg l^{-1}. This was diluted using ultra-pure water to 1 mg l^{-1}, before further dilution to make calibration standards of 0. 100, 250, 500, 750, and 1000 μg l^{-1}. Indium and scandium at a concentration of 100 μg l^{-1} were used as internal standards.

2.2.6. Upconversion luminescence

10 mg of as-prepared UCNPs in EtOH was added to a 1 cm path length quartz cuvette (111–10–40 QS, Hellma) and additional EtOH was added to adjust sample volume to 1 ml (i.e. a concentration of 10 mg ml^{-1}). The cuvette was gently shaken prior to each measurement to avoid UCNPs settling, the cuvette was then placed within a light-tight sample chamber for analysis. The excitation source was a femtosecond pulsed tuneable near-infrared laser (680–1300 nm, Coherent Discovery TPC, 100 fs, 80 MHz repetition rate, 1.2 mm spot size, maximum power of 1300 mW at 980 nm) which was routed to the sample chamber via suitable mirrors (BB1-EO3, Thorlabs) via tube enclosures. A spot-diameter on the sample of approximately 62 μm was achieved by focusing the beam with an ultrafast laser lens (11711, Edmund Optics). Our prior work indicates that the upconversion processes of PVP-UCNPs are saturated at these laser powers, but ultimately emission is maximised [17]. Excitation was detected and measured 90° to the excitation by an Ocean Optics HR2000Pro spectrometer (2048-pixel linear CCD Sony ILX5 chip, 200 μm slit, H3 grating, 350–850 nm spectral region). All measurements were conducted at 70% power, i.e. ~960 mW at 980 nm. 1000 spectra were accumulated per measurement, each of 50 ms integration time; operations were controlled via a custom-written LabVIEW program (LabVIEW 2013, NI). A 700 nm short-pass filter ensured that no stray excitation light reached the detector. Each UCNP emission spectrum was analysed using custom-written Matlab scripts (Matlab 2021b, Mathworks). Notably, each spectrum was smoothed using a shape-preserving Savitzky-Golay filtering algorithm to enhance clarity of the emission spectra (each spectrum was up-sampled to 10,000 data points; the Savitzky-Golay order was 5 and the Savitzky-Golay frame length was 55). Overall emission colour of each UCNP sample was quantified by calculating CIE 1931 chromaticity co-ordinates. For Er^{3+} doped samples, the green emission intensity was quantified by the total emission area under the curve arising from the $^2H_{11/2} \rightarrow {}^4I_{15/2}$ (~521 nm) and $^4S_{3/2} \rightarrow {}^4I_{15/2}$ (~545 nm) emission transitions, and red emission intensity was quantified as the total area under the emission curve of the $^4F_{9/2} \rightarrow {}^4I_{15/2}$ transition (~660 nm).

3. Results and discussion

STEM is used for visualising the core crystalline structure of the UCNPs (see figure 3) whereas SEM

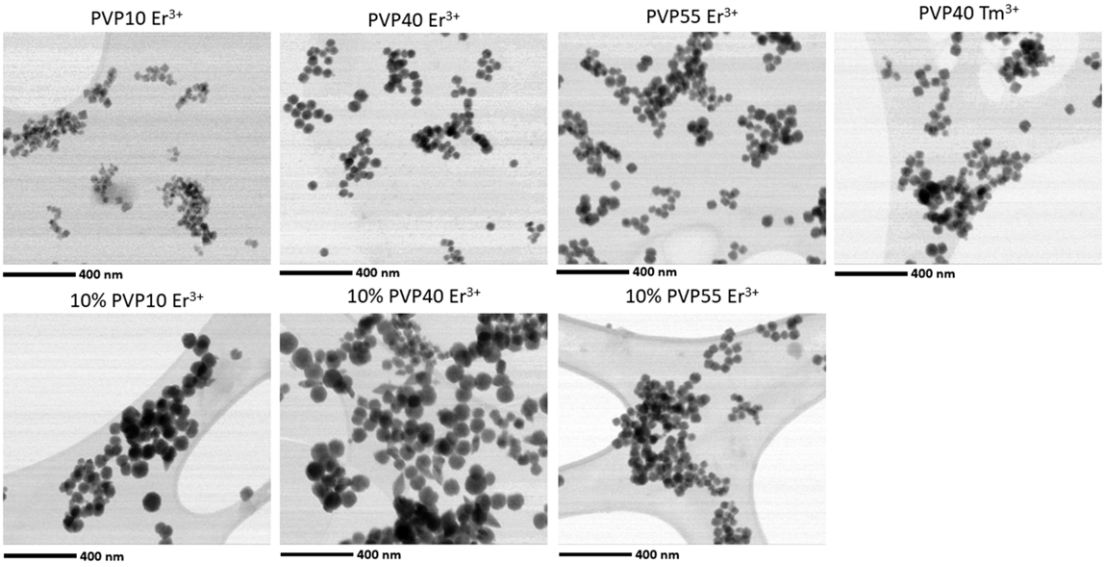

Figure 3. Representative STEM images of the UCNP samples produced. In all instances magnification is 100,000X and the scale bar represents 400 nm.

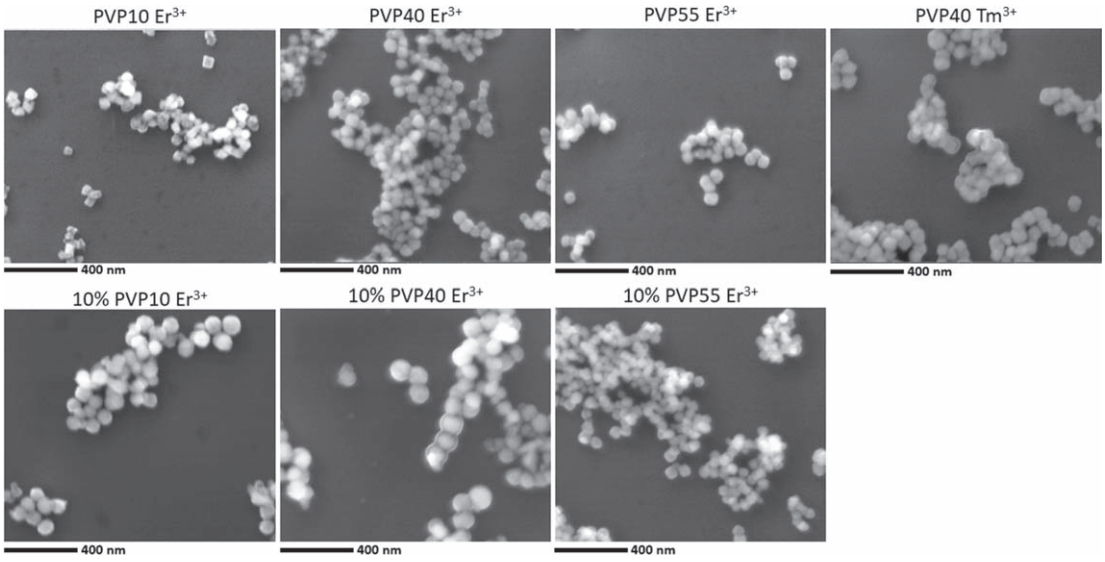

Figure 4. Representative SEM images of the UCNP samples produced. In all instances magnification is 100,000X and the scale bar is 400 nm.

imaging visualises the PVP coating around the UCNPs (see figure 4). The UCNPs produced were typically pseudo-spherical or pseudo-cuboid with varying diameters; these results are largely in-line with prior studies using the PVP-UCNP synthesis method [17]. Notably, a small number of unexpected rhombus-shaped UCNPs were observed in the 10% PVP10 Er^{3+} and 10% PVP40 Er^{3+} samples (see figure 5). HR-TEM images (shown in figure 6) indicated that the rhombus UCNPs appear to be flat, indicated by lower contrast than rhombus UCNPs compared to pseudo-spherical UCNPs. Further, that a crystal lattice can be observed in both pseudo-spherical and rhombus-shaped UCNPs. SEM images acquired at a 45° sample tilt may support the hypothesis that these rhombus-UCNPs are flat and not bipyramidal (see Supplementary figure 1), but these imaging experiments do not conclusively reveal the 3D morphology of the rhombus-shaped UCNPs. To further, investigate the crystal structure of individual nanoparticles, TKD measurements were performed on individual and clusters UCNPs. The inverse pole figure (IPF) map along the Z direction (which is the normal direction of the copper mesh) of a cluster of UNCPs (see figure 7(b)) indicates that all UCNPs were randomly orientated. Closer inspection of the diffraction patterns of rhombus-shaped (figures 7(c) and (d)) and pseudo-spherical UCNPs (figures 7(e) and (f)) shows that they were all of cubic (α-phase) crystalline structure. EDS analysis (see figure 8 and Supplementary figure 3) verified that all

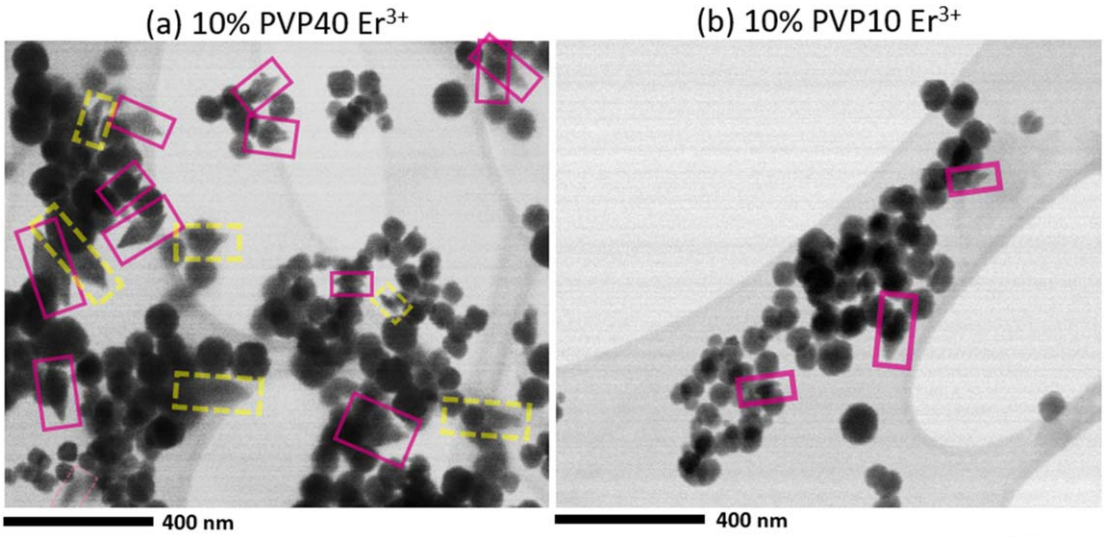

Figure 5. Observation of rhombus-shaped nanoparticle sub-populations in two samples . (a) STEM image of 10% PVP40 $NaYF_4$:Yb, Er UCNPs with clearly rhombus-shaped UCNPs highlighted with pink solid rectangles and pseudo-rhombus shapes highlighted in yellow dashed rectangles. Approximately 11% of nanoparticles were rhombus or psuedo-rhombus-shaped in this sample. (b) STEM image of 10% PVP10 $NaYF_4$:Yb,Er UCNPs with clearly rhombus-shaped UCNPs highlighted with pink solid rectangles. Pseudo-rhombus-shaped UCNPs were not observed in this sample. Approximately 4% of nanoparticles were rhombus-shaped in this sample.

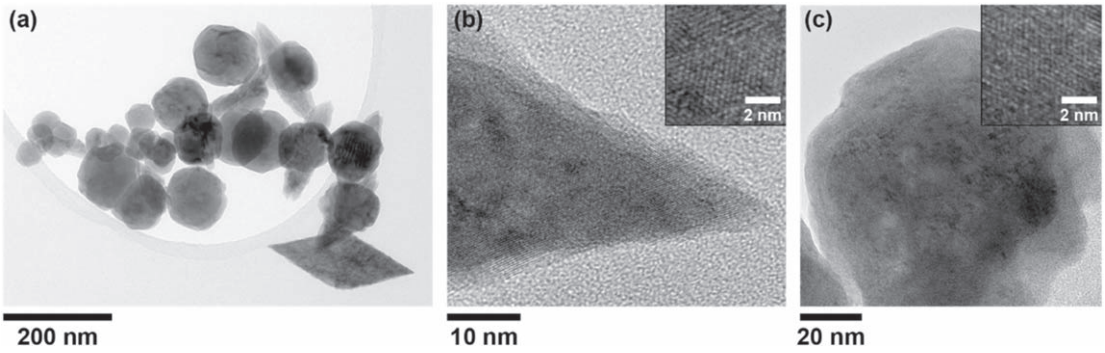

Figure 6. HR-TEM images of 10% PVP40 $NaYF_4$:Yb,Er UCNPs. (a) Representative image bright field of the sample showing rhombus and pseudo-spherical UCNPs. (b) Higher magnification bright field image of a rhombus-shaped UCNP where crystal lattice spacing can be seen (see further magnified insert). (c) as per (b), but for a pseudo-spherical UCNP.

nanoparticles produced contain Na, Y, F, Yb, and Er, as expected for the desired UCNPs. Therefore, the elemental composition and structure of individual rhombus-shaped UCNPs produced herein is consistent with UCNPs of other morphologies.

The synthesis of rhombus-shaped $NaYF_4$:Yb,Er UCNPs is notable for two reasons. Firstly, to the best of our knowledge, UCNPs with rhombus-like shapes have exclusively been observed in studies of $LiYF_4$ host-lattice UCNPs (where they may be referred to as 'bipyramidal' or 'octahedral' morphology, whether or not definitive 3D imaging has occurred). In such studies, populations of UCNPs are often exclusively rhombus/bipyramidal morphology, not a mixture of shapes. Hong *et al* (2017) attribute this rhombus morphology to UCNP formation via the tetragonal unit cell {101} plane [53]. Notably, these other rhombus UCNPs are grown via methods requiring high pressures and/or inert atmospheres [30, 53–63]. In contrast, the PVP-UCNP synthesis method requires much simpler and lower-cost equipment. However, only a small fraction of the UCNPs observed in 10% PVP10 and 10% PVP40 samples were rhombus-shaped, indicating multiple competing UCNP growth processes in these preparations. With the information available in this exploratory study, we are not able to elucidate a growth mechanism for the rhombus-shaped UCNP morphology with the information currently available. It is likely that parameters such as reaction time, reaction temperature, reaction pressure, and solvent choice will influence the production of rhombus-shaped PVP-nanoparticles in addition to the aforementioned affects of PVP molecular weight and the quantity of PVP used. It is not clear why rhombus UCNPs form for 10% PVP10 and 10% PVP40 samples, but not the 10% PVP55 sample, however Xia *et al* (2011) note that longer chain PVP (i.e. PVP55) may less efficiently adsorb and pack onto nanoparticle

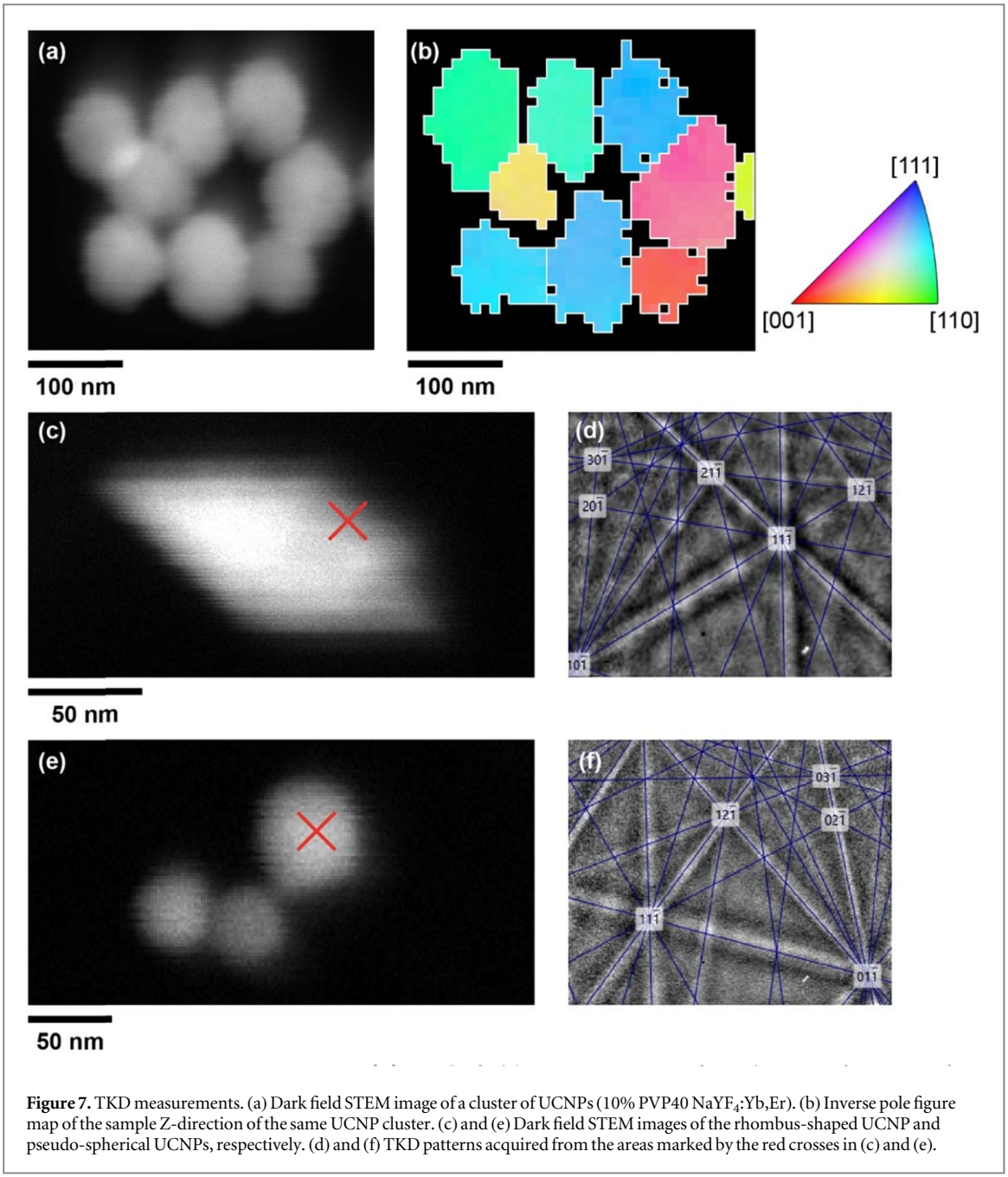

Figure 7. TKD measurements. (a) Dark field STEM image of a cluster of UCNPs (10% PVP40 $NaYF_4$:Yb,Er). (b) Inverse pole figure map of the sample Z-direction of the same UCNP cluster. (c) and (e) Dark field STEM images of the rhombus-shaped UCNP and pseudo-spherical UCNPs, respectively. (d) and (f) TKD patterns acquired from the areas marked by the red crosses in (c) and (e).

surfaces due to steric effects [2]. Control of UCNP morphology is particularly important for life sciences and biosensor applications, because (a) UCNP morphology determines uptake and translocation rates [64, 65], (b) the shape of UCNPs influences their Förster resonance energy transfer (FRET) response properties [66–68], and (c) the sharp edges of rhombus morphology may result in localised photothermal heating effects [55]. Further research is required to determine if rhombus-only UCNP populations can be produced by the PVP-assisted method.

Diameter measurements (see figure 9), revealed that incorporation of different PVP molecular weights in synthesis at nominal quantities resulted in only minor differences in UCNP diameter, all producing UCNPs with diameters in the range of ~55 nm. In contrast, reducing the quantity of PVP in the synthesis to 10% the nominal amount had a significant effect: the 10% PVP10 Er^{3+} and 10% PVP40 Er^{3+} UCNP samples, which were larger UCNPs on average with a dramatically wider spread of diameters than the samples using the nominal amount of PVP; i.e. 75 ± 24 nm and 93 ± 32 nm respectively, compared to an average of ~ 53 ± 11 nm for comparable samples. The exception to this is the PVP 55 Er^{3+} samples, which produced similar size distributions for both nominal and 10% PVP quantities. These results indicate that the quantity of PVP incorporated into synthesis must have a crucial role in controlling the morphology and diameter of UCNPs produced via the PVP-assisted route, e.g. an abundance of PVP may be necessary to control UCNP growth via a mechanism such as a

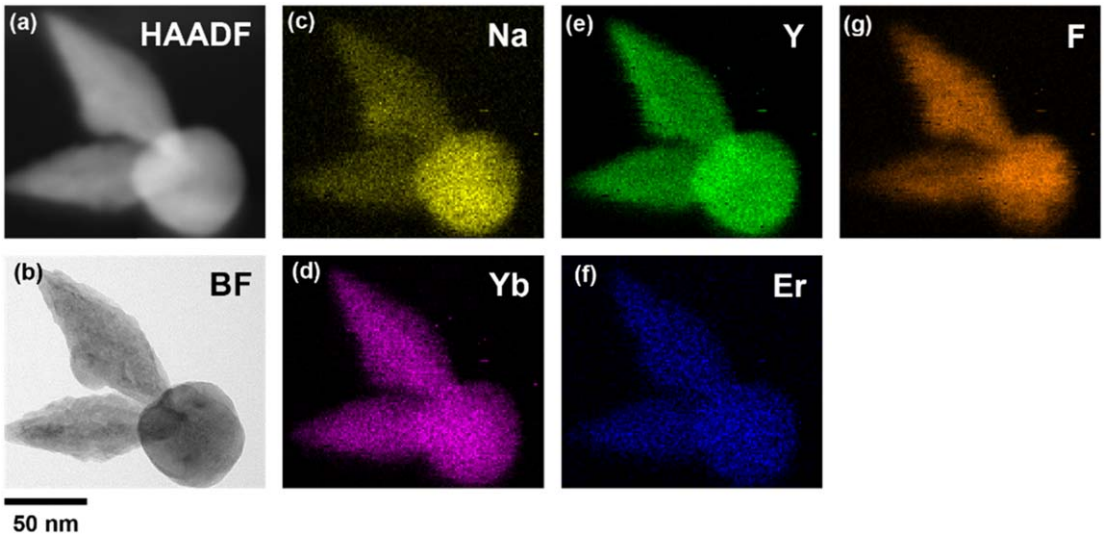

Figure 8. Elemental composition analysis using TEM EDS. (a) High-angle annular dark field (HAADF) and (b) bright field image of rhombus and pseudo-spherical nanoparticles (10% PVP10 $NaYF_4$:Yb,Er). (c - f) corresponding elemental maps.

templating effect, sequestering of precursors, or alteration of nucleation conditions. However, it is not clear from this exploratory study what mechanism(s) are involved and so carefully designed further studies are required to fully elucidate the role(s) PVP plays UCNP synthesis.

PXRD analysis of bulk powdered PVP-UCNP samples confirmed that all UCNPs conformed to cubic (α-phase) $NaYF_4$ crystalline lattice structure (see figure 10). There were some minor differences in crystal lattice parameter arising between each UCNP samples (see table 2), with the minimum being 5.490 $\pm$ 0.001 Å (PVP10 Er^{3+}) and maximum being 5.531 $\pm$ 0.001 Å (10% PVP40 Er^{3+}). ICP-MS measurement confirmed that all PVP Er^{3+} UCNP samples contained similar relative amounts of Y^{3+}, Yb^{3+}, and Er^{3+} (see table 3), indicating good inter-batch consistency.

Upconversion luminescence spectra exhibited by Er^{3+} UCNP samples (see figure 11 and Supplementary figure 2) were generally in accordance to that reported by Li and Zhang (2006) [3], where red and green emission ratios close to parity was obtained. The 10% PVP55 Er^{3+} UCNPs exhibited the somewhat brighter emission relative to the other samples, although there is no clear reason for this slight enhancement in luminescence. Factors such as morphology-dependent solvent quenching, unit cell volume, and UCNP order could feasibly play a role, but no clear trend is evident [45]. The PVP40 Er^{3+} UCNP samples provides a notable opportunity for direct inter-study comparison. Notably the value of crystal lattice parameter, *a*, obtained for PVP40 Er^{3+} was identical to those produced by Sikora *et al* 2013 [6] and MacKenzie *et al* 2022 [17] (i.e. 5.52 Å), indicating excellent inter-study repeatability. However, the PVP40 Er^{3+} UCNPs produced in this study exhibited a relatively low red/green emission ratio of 0.77, which is considerably less than the red/green ratio achieved in MacKenzie *et al* (2022) and Sikora *et al* (2013) (i.e. approximately ~3) [6, 17]. Furthermore, the PVP40 Er^{3+} UCNPs produced in this study were significantly larger than those produced by MacKenzie *et al* (2022) (i.e. 52 $\pm$ 10 nm versus 42 $\pm$ 11 nm respectively) [17]. Whilst there are trivial reasons for inter-study differences, e.g. operator variability, differences in glassware or heating medium, the most likely reason for these inter-study difference to have arisen is use of a different hotplate stirrer apparatus, which will have imbued a different heating rate to the prior study. MacKenzie *et al* used an IKA RCT basic hotplate/stirrer and this study used a Fisherbrand™ AREX with VTF hotplate/stirrer. Notably, both these hotplates have different temperature-cotrol logic which cannot be matched. Heating rate is known to be an important parameter in UCNP synthesis [69, 70]. Indeed, a recent exemplary study on reproducible UCNP synthesis by Andresen *et al* identified heating rate as a key parameter [34]. We hypothesise that heating rate may affect order within UCNPs, therefore influencing UCNP optical properties even where otherwise identical unit-cell parameters have been obtained.

From this exploratory study, it is not clear if the rhombus-shaped nanoparticles have different properties from the pseudo-spherical nanoparticles produced. Discerning the optical behaviour of individual UCNPs require upconversion studies of single nanoparticles, which would necessitate super-resolution optical microscopy approaches, however it is not clear if such approaches could discriminate between rhombus and pseudo-spherical UCNPs [71]. Therefore producing populations of exclusively rhombus-shaped UCNPs would be most desirable for straight-forward understanding of the optical properties of rhombus-shaped PVP-UCNPs.

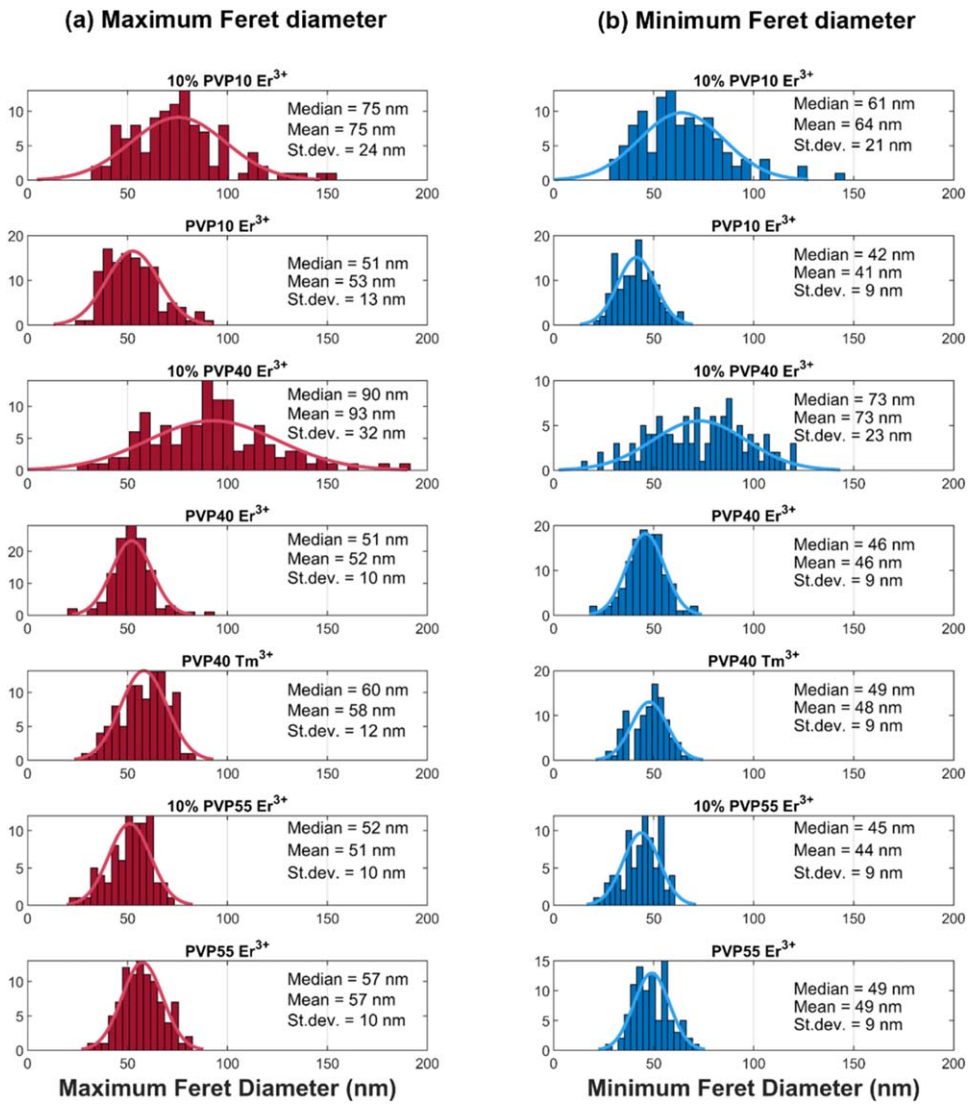

Figure 9. Diameter of UCNP populations. (a) Maximum Feret diameters. (b) Minimum Feret diameters. Fits are Gaussian (normal) distributions.

Notably, overall upconversion emission intensity from PVP40 Tm^{3+} UCNPs was much stronger than any of the Er^{3+} UCNPs, with strong blue (~474 nm) and strong red emission (~660 nm) (see figure 11). Whilst the PVP40 Tm^{3+} UCNPs were around 11% larger in diameter than PVP40 Er^{3+} UCNPs, they displayed a somewhat reduced crystal lattice parameter, *a*, of 5.502 ± 0.03 Å compared to 5.524 ± 0.001 Å for the PVP40 Er^{3+} UCNPs. Furthermore, ICP-MS revealed that the PVP40 Tm^{3+} UCNPs incorporated a slightly reduced amount of photonically inert Y^{3+} (3.6 relative % less) and a slightly increased amount of photonically active Yb^{3+} (3.2 relative % more) compared to the average of Er^{3+} containing UCNPs (see table 3). It is not clear why the PVP40 Tm^{3+} UCNPs incorporated proportionally more Yb^{3+}, but other studies have noted that increasing Yb^{3+} can increase emission intensity [6]. Therefore increased upconversion emission from the PVP40 Tm^{3+} UCNPs could possibly be explained by a greater density of Yb^{3+} ions and reduced inter-ion separation [6, 72]. When plotted on a CIE 1931 chromaticity diagram, the PVP Tm^{3+} UCNPs yield apparent purple emission. This contrasts results by Li and Zhang (2006), whose PVP40 Tm^{3+} UCNPs exhibited strong blue and relatively weaker red emission (~650 nm) [$^1G_4 \rightarrow {}^3F_4$ and $^3F_3 \rightarrow {}^3H_6$ emission transitions]. It should also be noted that the PVP40 Tm^{3+} UCNPs may also exhibit luminescence ~800 nm which could not be recorded with the instrumentation used in this study [23]. Overall, these results demonstrate that PVP40 Tm^{3+} UCNPs with strong dual-band blue and red emission properties can be produced via the PVP-assisted route.

The limitations of this study should be acknowledged. Firstly, only three PVP molecular weights were tested. A wider range of PVP molecular weights are commercially available, but these have different bulk properties (e.g. higher molecular weight PVP samples are poorly soluble in ethylene glycol), and so would have required modification of the experimental

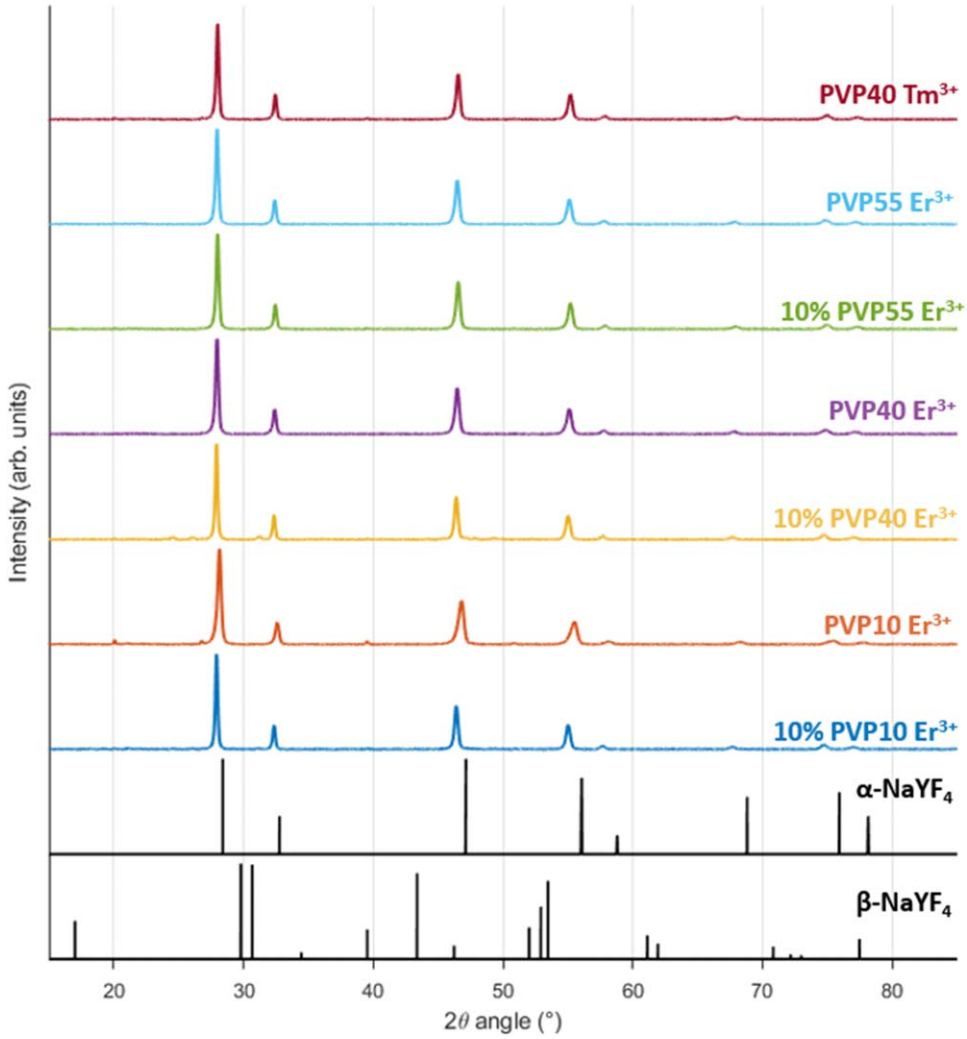

Figure 10. PXRD patterns of bulk dry powder indicate that UCNP unit cell structure conforms to cubic (α-phase) $NaYF_4$ for all samples.

Table 2. Crystal lattice parameters calculated for each UCNP sample.

Sample	Crystal lattice	
parameter, *a*. (Å)	Literature Value(s)	
PVP10 Er^{3+}	5.490 ± 0.001	—
10% PVP10 Er^{3+}	5.531 ± 0.001	—
PVP40 Er^{3+}	5.524 ± 0.001	5.521 ± 0.003 (MacKenzie *et al*) [17] 5.52 (Sikora *et al*) [6]
10% PVP40 Er^{3+}	5.531 ± 0.001	—
PVP55 Er^{3+}	5.520 ± 0.002	—
10% PVP55 Er^{3+}	5.515 ± 0.001	—
PVP40 Tm^{3+}	5.502 ± 0.003	—

protocol (e.g. heating to aid polymer solubility) which is not conducive for this initial comparative study. Additionally, hybrid mixtures of different PVP molecular weights and hybrid solvent compositions were not explored. Secondly, only two quantities of PVP were investigated: the nominal amount (574 mg) and 10% of the nominal amount (57.4 mg); different quantities of PVP may yield differing results and should be explored in future. Additionally, the long-term stability of PVP-UCNPs has not been studied [73, 74]. Thermogravimetric analysis may be useful for studying the relative amount of PVP contained in each UCNP sample [1]. Thirdly, this work was conducted using lanthanide oxide starting materials; prior work indicated that using other starting materials (particularly lanthanide nitrates) may disrupt nanoparticle formation, perhaps due to varying nucleation interactions with the PVP [17]. Solution-state studies of directly excited lanthanide luminescence may be required to study the relevant processes involved.

Table 3. Relative amounts (%) of photonically active elements in each sample, calculated from ICP-MS data. N.B. uncertainties arising from three repeated measurements were negligible and so are not quoted.

Sample	Y 89 (%)	Yb 172 (%)	Er 166 (%)	Tm 169 (%)
PVP10 Er^{3+}	64.8	32.4	2.8	0.0
10% PVP10 Er^{3+}	65.0	32.3	2.7	0.0
PVP40 Er^{3+}	64.6	32.7	2.8	0.0
10% PVP40 Er^{3+}	64.7	32.4	2.9	0.0
PVP55 Er^{3+}	64.4	32.6	3.0	0.0
10% PVP55 Er^{3+}	65.2	32.1	2.7	0.0
Mean ± std. dev. of above	64.8 ± 0.3	32.4 ± 0.2	2.8 ± 0.1	0.0
PVP40 Tm^{3+}	61.2	35.6	0.0	3.1

Fourthly, whilst open-to-air synthesis is an advantage, degassing the reaction solution to purge oxygen may enhance UCNP luminescence by enhancing crystal purity of UCNPs [75]. Additionally, further optical studies, e.g. of quantum yield and of emission from single UCNP would be beneficial to the understanding PVP-UCNPs [46, 76]. Overall, there is ample room for further fundamental investigations of PVP-UCNPs.

4. Conclusions

In this exploratory study, we have demonstrated that altering PVP molecular weight and PVP amount used in synthesis can influence the morphology and diameter of cubic (α-phase) $NaYF_4$:Yb,Er UCNPs produced via a modest-temperature open-to-air synthesis route. The choice of PVP molecular weight (i.e. 10,000, 40,000, 50,000 kDa) had minimal effect on resulting UCNP size distributions when incorporated in synthesis at nominal amounts. However, reducing the quantity of PVP10 and PVP40 to 10% of the nominal amount produced much wider size distributions of UCNPs, with a notable sub-population of rhombus-shaped UCNPs. The exception to this were the samples incorporate ng PVP55, where the difference arising from varying PVP amount was marginal. Notably, a small fraction of rhombus-shaped $NaYF_4$:Yb,Er UCNPs were produced in the 10% PVP40 Er^{3+} and 10% PVP10 Er^{3+} samples (~11% and ~4% of total UCNPs respectively). Single nanoparticle structural and elemental analysis supports the conclusion that these rhombus-shaped nanoparticles were cubic (α-phase) $NaYF_4$:Yb,Er UCNPs. Rhombus-shaped UCNPs were not observed in PVP55 samples. Despite these intriguing results, the mechanism for how PVP influences the growth of UCNPs has not been elucidated by this exploratory study, with templating and precursor sequestering being plausible effects. Ultimately, further work is required to fully understand and exploit the potential of PVP in UCNP synthesis.

In broader context, the PVP-assisted route of UCNP synthesis is promising but remains largely unexploited despite it's inherent advantages of modest reaction temperatures, open-to-air synthesis, and simple equipment requirements. The full range of UCNP morphologies and photonic emission properties that can be produced by altering PVP parameters remains to be established, with critical reaction parameters of synthesis temperature, synthesis pressure, reaction time, reaction atmosphere, and solvent choice yet to be explored. To-date, the PVP-assisted UCNP synthesis route has produced UCNPs with blue and red emission ($NaYF_4$:Yb,Tm), green/red emission ($NaYF_4$:Yb,Er), and strong red emission ($NaYF_4$:Yb,Er,Mn). Further investigation of host lattice, lanthanide, and transition metal dopant combinations could enhance emission properties and unlock further desirable emission wavebands. Indeed, the potential for scaled-up production and multi-colour UCNP populations indicates that the PVP-assisted route could be particularly useful for large-scale UCNP applications, such as display technologies and stochastically-patterned nano-security inks.

Funding and acknowledgments

L M is supported by a Biotechnology and Biological Sciences Research Council (BBSRC) Discovery Fellowship (BB/T009268/1). R P is supported by a Royal Society University Research Fellowship (URF/R/191002 and RF\ERE\210091) and a BBSRC award (BB/S017615/1 and BB/X001172/1). This work was enabled by a Royal Society Research Grant (RGS\R1\221139). JB is supported by a Royal Society of Edinburgh (RSE) Saltire International Collaboration Award (1917).

The authors would like to gratefully acknowledge the following people for their assistance and contributions that made this work possible. Dr Paul R. Edwards and Professor Robert W. Martin (Department of Physics, University of Strathclyde) for access to and assistance with STEM and SEM. Dr Tanya Peshkur and Mara Knapp (Civil and Environmental Engineering, University of Strathclyde) for assistance with sample digestion for ICP-MS. Alex Clunie (Department of Pure and Applied Chemistry, University of Strathclyde) for assistance with ICP-MS. Dr Lauren E. Hatcher (School of Chemistry, Cardiff University) for helpful discussions. PXRD measurements were carried out in the CMAC National Facility, housed within the University of Strathclyde's Technology and Innovation Centre, and funded with a UKRPIF (UK Research Partnership Institute Fund) capital award, SFC ref. H13054, from the Higher Education Funding Council for England (HEFCE). We thank Dr Alan Martin of CMAC for assistance with PXRD measurements and Blair Welsh from Coherent UK Ltd for their invaluable help with regard to NIR laser system

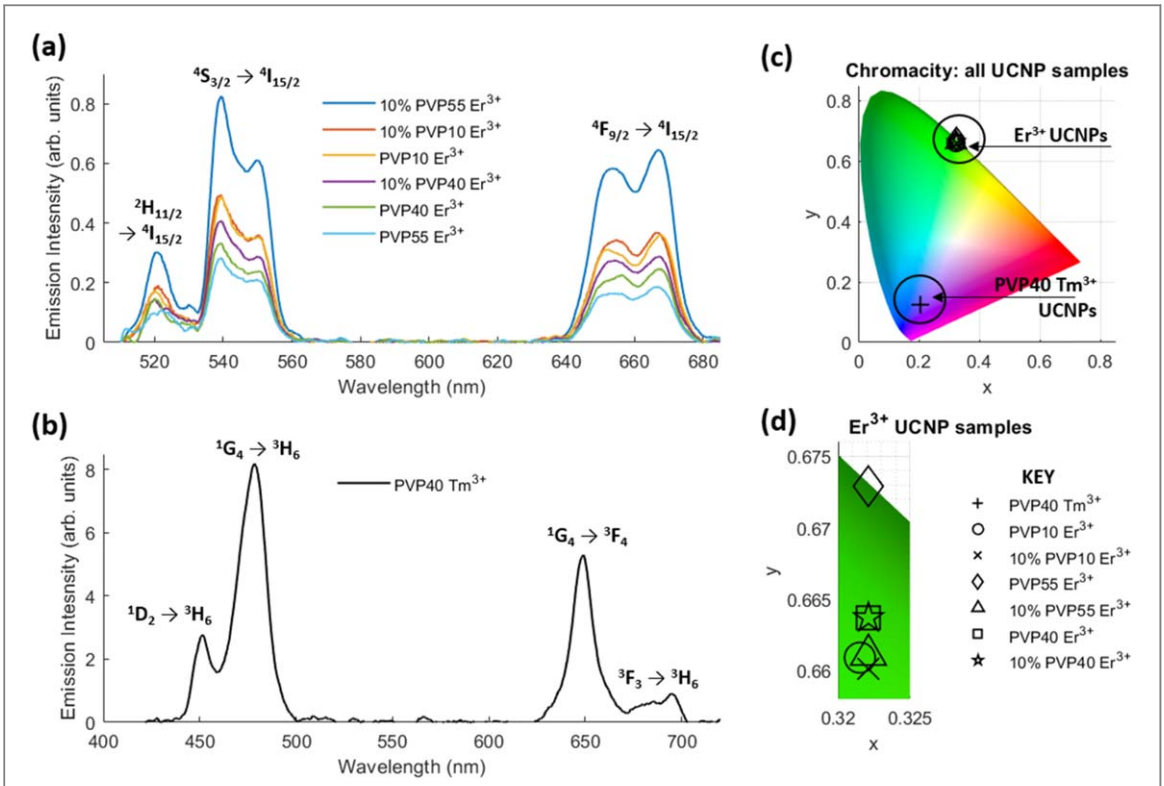

Figure 11. UCNP emission properties. (a) Upconversion luminescence emission spectra for Er^{3+} doped PVP-UCNPs samples (10 mg ml^{-1} in EtOH), excited at 980 nm. (b) Upconversion luminescence emission spectra for the PVP40 Tm^{3+} UCNP sample. (c) CIE 1931 chromaticity diagram for all UCNP samples. (d) Enhanced view of CIE 1931 chromaticity plot showing the difference between Er^{3+} doped UCNPs.

used throughout. Additional thanks to Dr Artiom Skripka for the helpful suggestion to study the elemental composition of single UCNPs at SHIFT 22 conference (October 2022, Tenerife). We would like to thank the conference organisers for SHIFT 22 and Methods and Application of Fluorescence 2022 for running such welcoming and engaging conferences. Finally, we would like to thank the two anonymous peer-reviewers whose thorough contribution improved this manuscript considerably.

The authors have declared that no conflicting interests exist.

Data availability statement

The data that support the findings of this study are openly available at the following URL/DOI: https://doi.org/10.6084/m9.figshare.22434913.v1.

Author contributions

- R B Synthesised all UCNP samples, contributed to experimental design and methodology, conducted preliminary analysis of PXRD, SEM, and upconversion luminescence data.
- J B Conducted the TKD measurements and associated analysis, created Figures, and contributed to writing of the manuscript, and reviewed the manuscript.
- M G Conducted high-resolution TEM imaging and EDS measurements.
- G C Conducted the TKD measurements and reviewed the manuscript.
- R P Conducted upconversion luminescence emission measurements and reviewed the manuscript.
- L M Secured funding, conceived the project and methodology, conducted STEM and SEM imaging, analysed the data, produced figures, curated data, and wrote the manuscript.
- All authors gave final approval for publication.

ORCID iDs

Jochen Bruckbauer https://orcid.org/0000-0001-9236-9320
Grzegorz Cios https://orcid.org/0000-0003-4269-5456
Robert Pal https://orcid.org/0000-0002-0641-4218
Lewis E MacKenzie https://orcid.org/0000-0002-8151-0525

References

[1] Koczkur K M, Mourdikoudis S, Polavarapu L and Skrabalak S E 2015 Polyvinylpyrrolidone (PVP) in nanoparticle synthesis *Dalton Trans.* **44** 17883–905

[2] Xia X, Zeng J, Oetjen L K, Li Q and Xia Y 2011 Quantitative analysis of the role played by poly(vinylpyrrolidone) in seed-mediated growth of Ag nanocrystals *JACS* **134** 1793–801

[3] Li Z and Zhang Y 2006 Monodisperse silica-coated polyvinyl-pyrrolidone/NaYF4 nanocrystals with multicolor upconversion fluorescence emission *Angewandte Chemie - International Edition* **45** 7732–5

[4] Liu C *et al* 2014 The action mechanism of TiO_2:NaYF4:Yb3+,Tm3+ cathode buffer layer in highly efficient inverted organic solar cells *Appl. Phys. Lett.* **105** 53301

[5] Grüner M C, Arai M S, Carreira M, Inada N and De Camargo A S S 2018 Functionalizing the mesoporous silica shell of upconversion nanoparticles to enhance bacterial targeting and killing via photosensitizer-induced antimicrobial photodynamic therapy *ACS Applied Bio Materials* **1** 1028–36

[6] Sikora B *et al* 2013 Transport of NaYF4:Er3+, Yb3+ up-converting nanoparticles into HeLa cells *Nanotechnology* **24** 235702

[7] Menyuk N, Dwight K and Pierce J W 1972 NaYF4: Yb,Er - An efficient upconversion phosphor *Appl. Phys. Lett.* **21** 159–61

[8] Mackenzie L E *et al* 2018 The theoretical molecular weight of NaYF4:RE upconversion nanoparticles *Sci. Rep.* **8** 1106

[9] Shi F, Wang J, Zhai X, Zhao D and Qin W 2011 Facile synthesis of β-NaLuF 4 :Yb/Tm hexagonal nanoplates with intense ultraviolet upconversion luminescence *CrystEngComm* **13** 3782–7

[10] Chen B and Wang F 2020 Recent advances in the synthesis and application of Yb-based fluoride upconversion nanoparticles *Inorg. Chem. Front.* **7** 1067–81

[11] Nampi P P *et al* 2021 Barium yttrium fluoride based upconversion nanoparticles as dual mode image contrast agents *Mater. Sci. Eng.,* **124** 111937

[12] Cheng T, Marin R, Skripka A and Vetrone F 2018 Small and bright lithium-based upconverting nanoparticles *J. Am. Chem. Soc.* **140** 12890–9

[13] Przybylska D and Grzyb T 2020 Synthesis and up-conversion of core/shell SrF2:Yb3+,Er3+@SrF2:Yb3+,Nd3+ nanoparticles under 808, 975, and 1532 nm excitation wavelengths *J. Alloys Compd.* **831** 154797

[14] Ramírez-García G *et al* 2019 A turn-on luminescence method for phosphate determination based on fast green-functionalized ZrO_2:Yb,Er@ZrO_2 core@shell upconversion nanoparticles *Anal. Chem.* **91** 14657–65

[15] Mahata M K, Kumar K and Rai V 2015 Kr. Er3+–Yb3+ doped vanadate nanocrystals: a highly sensitive thermographic phosphor and its optical nanoheater behavior *Sensors Actuators B* **209** 775–80

[16] Silva F R O *et al* 2022 Lanthanide-based β-tricalcium phosphate upconversion nanoparticles as an effective theranostic nonviral vectors for image-guided gene therapy *Nanotheranostics* **6** 306–21

[17] Mackenzie L E, Mackenzie L E, Alvarez-ruiz D and Pal R 2022 Low-temperature open-air synthesis of PVP-coated $NaYF_4$: Yb , Er , Mn upconversion nanoparticles with strong red emission *Royal Society Open Science* **9** 211508

[18] Chan E M *et al* 2012 Combinatorial discovery of lanthanide-doped nanocrystals with spectrally pure upconverted emission *Nano Lett.* **12** 3839–45

[19] The Coming of Age of Neodymium: Redefining Its Role in Rare Earth Doped Nanoparticles 2022 *Chemical Reviews* **123** 515–54

[20] Tang J *et al* 2015 Selectively enhanced red upconversion luminescence and phase/size manipulation via Fe3+ doping in $NaYF_4$:Yb,Er nanocrystals *Nanoscale* **7** 14752–9

[21] Idris N M *et al* 2009 Tracking transplanted cells in live animal using upconversion fluorescent nanoparticles *Biomaterials* **30** 5104–13

[22] He H *et al* 2018 Quantitative lateral flow strip sensor using highly doped upconversion nanoparticles *Anal. Chem.* **90** 12356–60

[23] Wang N, Yu X, Zhang K, Mirkin C A and Li J 2017 Upconversion nanoprobes for the ratiometric luminescent sensing of nitric oxide *JACS* **139** 12354–7

[24] Liu Y *et al* 2020 Super-resolution mapping of single nanoparticles inside tumor spheroids *Small* **16** 1905572

[25] Mun K R *et al* 2023 Elemental-migration-assisted full-color-tunable upconversion nanoparticles for video-rate three-dimensional volumetric displays *Nano Letters* **23** 3014–22

[26] Meruga J M *et al* 2018 Stable inks containing upconverting nanoparticles based on an oil-in-water nanoemulsion *Langmuir* **34** 1535–41

[27] Lee J *et al* 2017 Ultra-wideband multi-dye-sensitized upconverting nanoparticles for information security application *Adv. Mater.* **29** 1603169

[28] Geitenbeek R G *et al* 2017 $NaYF_4$:Er 3+, Yb 3+/SiO_2 core/shell upconverting nanocrystals for luminescence thermometry up to 900 K *J. Phys. Chem. C* **11** 46

[29] Meng F *et al* 2012 Open-circuit voltage enhancement of inverted polymer bulk heterojunction solar cells by doping $NaYF_4$ nanoparticles/PVP composites *J. Mater. Chem.* **22** 22382

[30] Hong A-R, Kyhm J-H, Kang G and Jang H S 2021 Orthogonal R/G/B upconversion luminescence-based full-color tunable upconversion nanophosphors for transparent displays *Nano Lett.* **21** 4838–44

[31] Gao L *et al* 2020 Video-rate upconversion display from optimized lanthanide ion doped upconversion nanoparticles *Nanoscale* **12** 18595–9

[32] Meruga J M *et al* 2012 Security printing of covert quick response codes using upconverting nanoparticle inks *Nanotechnology* **23** 395201

[33] Fu X *et al* 2022 Excitation energy mediated cross-relaxation for tunable upconversion luminescence from a single lanthanide ion *Nat. Commun.* **13** 4741

[34] Andresen E *et al* 2023 Assessing the reproducibility and up-scaling of the synthesis of Er,Yb-doped NaYF4-based upconverting nanoparticles and control of size, morphology, and optical properties *Sci Rep.* **13** 2288

[35] Chen J *et al* 2012 Controllable synthesis of NaYF4 : Yb,Er upconversion nanophosphors and their application to *in vivo* imaging of Caenorhabditis elegans† *J. Mater. Chem.* **21** 1–16

[36] Amouroux B *et al* 2019 Importance of the mixing and high-temperature heating steps in the controlled thermal coprecipitation synthesis of sub-5-nm Na(Gd−Yb)F 4 :Tm *Inorg. Chem.* **58** 5082–8

[37] Halimi I *et al* 2019 Pick your precursor! Tailoring the size and crystal phase of microwave-synthesized sub-10 nm upconverting nanoparticles *J. Mater. Chem.* **7** 15364–74

[38] Panov N, Marin R and Hemmer E 2018 Microwave-assisted solvothermal synthesis of upconverting and downshifting rare-earth-doped LiYF4 microparticles *Inorg. Chem.* **57** 14920–9

[39] Lei P *et al* 2017 Ultrafast synthesis of novel hexagonal phase NaBiF4 upconversion nanoparticles at room temperature *Adv. Mater.* **29** 4–7

[40] Shao B *et al* 2014 A novel synthetic route towards monodisperse β-NaYF4:Ln3+ micro/nanocrystals from layered rare-earth hydroxides at ultra low temperature *Chem. Commun.* **50** 12706–9

[41] Mackenzie L E and Pal R 2020 Circularly polarized lanthanide luminescence for advanced security inks *Nature Reviews Chemistry* **5** 109–24

[42] Arppe R and Sørensen T J 2017 Physical unclonable functions generated through chemical methods for anti-counterfeiting *Nature Reviews Chemistry* **1** 0031

[43] Sivakumar M, Kanagesan S, Umapathy V, Suresh Babu R and Nithiyanantham S 2013 Study of $CoFe_2O_4$ particles synthesized with various concentrations of PVP polymer *J. Supercond. Novel Magn.* **26** 725–31

[44] Sikora B *et al* 2017 Mammalian cell defence mechanisms against the cytotoxicity of $NaYF_4$:(Er,Yb,Gd) nanoparticles *Nanoscale* **9** 14259

[45] Arppe R *et al* 2015 Quenching of the upconversion luminescence of NaYF 4 :Yb 3+ , Er 3+ and $NaYF_4$:Yb 3+ , Tm 3+ nanophosphors by water: the role of the sensitizer Yb 3 + in non-radiative relaxation *Nanoscale* **7** 11746–57
[46] Quintanilla M, Hemmer E, Marques-hueso J, Rohani S and Lucchini G 2022 Cubic versus Hexagonal—Phase *Size and Morphology Effects on the Photoluminescence Quantum Yield of.* **5** 1–25
[47] Schneider C a, Rasband W S and Eliceiri K W 2012 NIH Image to ImageJ: 25 years of image analysis *Nat. Methods* **9** 671–5
[48] Schindelin J *et al* 2012 Fiji: an open-source platform for biological-image analysis *Nat. Methods* **9** 676–82
[49] Keller R R and Geiss R H 2012 Transmission EBSD from 10 nm domains in a scanning electron microscope *J. Microsc.* **245** 245–51
[50] Trimby P W 2012 Orientation mapping of nanostructured materials using transmission Kikuchi diffraction in the scanning electron microscope *Ultramicroscopy* **120** 16–24
[51] Tokarski T *et al* 2021 Transmission kikuchi diffraction: the impact of the signal-to-noise ratio *Ultramicroscopy* **230** 113372
[52] Bachmann F, Hielscher R and Schaeben H 2010 Texture analysis with MTEX—Free and open source software toolbox *Solid State Phenomena* **160** 63–8
[53] Hong A R, Kim S Y, Cho S H, Lee K and Jang H S 2017 Facile synthesis of multicolor tunable ultrasmall LiYF4:Yb,Tm,Er/LiGdF4 core/shell upconversion nanophosphors with sub-10 nm size *Dyes Pigm.* **139** 831–8
[54] Marin R *et al* 2018 Upconverting nanoparticle to quantum dot förster resonance energy transfer: increasing the efficiency through donor design *ACS Photonics* **5** 2261–70
[55] Na H *et al* 2014 Facile synthesis of intense green light emitting LiGdF 4 :Yb,Er-based upconversion bipyramidal nanocrystals and their polymer composites† *Nanoscale* **6** 7461
[56] Qiao Y *et al* 2021 Plant tissue imaging with bipyramidal upconversion nanocrystals by introducing Tm3+ions as energy trapping centers *Nanoscale* **13** 8181–7
[57] Kim S Y, Jeong J S, Mkhoyan K A and Jang H S 2016 Direct observation of the core/double-shell architecture of intense dual-mode luminescent tetragonal bipyramidal nanophosphors *Nanoscale* **8** 10049–58
[58] Shin J, Kim Y, Lee J, Kim S and Jang H S 2017 Highly Bright and Photostable Li(Gd,Y)F4:Yb,Er/LiGdF4 Core/Shell Upconversion Nanophosphors for Bioimaging Applications *Part. Part. Syst. Char.* **34** 1600183
[59] Yang D *et al* 2012 Synthesis of $Li_{1-x}Na_xYF_4$:Yb^{3+} /Ln^{3+} ($0 \leq x \leq 0.3$, Ln = Er, Tm, Ho) nanocrystals with multicolor upconversion luminescence properties for *in vitro* cell imaging† *Journal of Materials Chemistry* **22** 20618
[60] Wang M *et al* 2014 Lanthanide-doped upconversion nanoparticles electrostatically coupled with photosensitizers for near-infrared-triggered photodynamic therapy *Nanoscale* **6** 8274–82
[61] Min Q *et al* 2020 Atomic-level passivation of individual upconversion nanocrystal for single particle microscopic imaging *Adv. Funct. Mater.* **30** 1–7
[62] Chung Y C, Yang C H, Lee R H and Wang T L 2019 Dual stimuli-responsive block copolymers for controlled release triggered by upconversion luminescence or temperature variation *ACS Omega* **4** 3322–8
[63] Chien H W, Yang C H, Tsai M T and Wang T L 2020 Photoswitchable spiropyran-capped hybrid nanoparticles based on UV-emissive and dual-emissive upconverting nanocrystals for bioimaging *J. Photochem. Photobiol., A* **392** 112303
[64] Nordmann J, Buczka S, Voss B, Haase M and Mummenhoff K 2015 *In vivo* analysis of the size-and time-dependent uptake of NaYF4 :Yb,Er upconversion nanocrystals by pumpkin seedlings *J. Mater. Chem.* **3** 144–50
[65] Zhang D *et al* 2018 The morphology and surface charge-dependent cellular uptake efficiency of upconversion nanostructures revealed by single-particle optical microscopy† *Chem. Sci.* **9** 5260
[66] Das A, Corbella Bagot C, Rappeport E, Tis T B and Park W 2021 Quantitative modeling and experimental verification of Förster resonant energy transfer in upconversion nanoparticle biosensors *J. Appl. Phys.* **130** 23102
[67] Chen T, Shang Y, Zhu Y, Hao S and Yang C 2022 Activators confined upconversion nanoprobe with near-unity förster resonance energy transfer efficiency for ultrasensitive detection *ACS Appl. Mater. Interfaces* **14** 19826–35
[68] Francés-Soriano L, Estebanez N, Pérez-Prieto J and Hildebrandt N 2022 DNA-coated upconversion nanoparticles for sensitive nucleic acid FRET biosensing *Adv. Funct. Mater.* **32** 2201541
[69] Egatz-Gomez A, Asher M, Peterson R, A. Roldan M and Ros A 2022 Microwave synthesis of upconverting nanoparticles with bis(2-ethylhexyl) adipate *RSC Adv.* **12** 23026–38
[70] Kavand A *et al* 2021 Controlled synthesis of NaYF4 :Yb,Er upconversion nanocrystals as potential probe for bioimaging: a focus on heat treatment *Applied Nano Materials* **4** 5319–29
[71] Chen C *et al* 2018 Multi-photon near-infrared emission saturation nanoscopy using upconversion nanoparticles *Nat. Commun.* **9** 3290
[72] Punjabi A *et al* 2014 Amplifying the red-emission of upconverting nanoparticles for biocompatible clinically used prodrug-induced photodynamic therapy *ACS Nano* **8** 10621–30
[73] Märkl S, Schroter A and Hirsch T 2020 Small and bright water-protected upconversion nanoparticles with long-time stability in complex, aqueous media by phospholipid membrane coating *Nano Lett.* **20** 8620–5
[74] Plohl O *et al* 2016 Optically detected degradation of NaYF4: Yb, Tm based upconversion nanoparticles in phosphate buffered saline solution *Langmuir acs.langmuir.* **33** 553–60
[75] Krämer K W *et al* 2004 Hexagonal sodium yttrium fluoride based green and blue emitting upconversion phosphors *Chem. Mater.* **16** 1244–51
[76] Zhou J, Xu S, Zhang J and Qiu J 2015 Upconversion luminescence behavior of single nanoparticles *Nanoscale* **7** 15026–36